# THERMAL FREEZE-OUT VERSUS CHEMICAL FREEZE-OUT REEXAMINED

Dariusz Prorok

Institute of Theoretical Physics, University of Wrocław
Pl. Maksa Borna 9, 50-204 Wrocław, Poland

*(Received June 23, 2009; revised version received August 21 2009)*

An alternative, to the commonly used blast-wave, model describing the freeze-out hypersurface is applied to fit the $p_{\mathrm{T}}$-spectra of identified hadrons measured at relativistic heavy-ion collisions at $\sqrt{s_{\mathrm{NN}}} = 62.4, 130$ and 200 GeV. Decays of resonances are taken into account completely. It has turned out that the fitted freeze-out temperature and baryon number chemical potential depend weakly on the centrality of the collision and their values are close to the chemical freeze-out values determined from fits to particle yield ratios.

PACS numbers: 25.75.–q, 25.75.Dw, 24.10.Pa, 24.10.Jv

## 1. Introduction

During a heavy-ion collision a hot and dense medium is created which eventually evolves into a state of freely streaming particles. The process of hadron decoupling is called freeze-out and two kinds of freeze-out are distinguished [1, 2]: *(i) chemical freeze-out* at $T_{\mathrm{chem}}$ when the hadron abundances become fixed, *(ii) thermal (kinetic) freeze-out* at $T_{\mathrm{kin}}$ when elastic rescattering processes cease and hadrons start to escape freely and $T_{\mathrm{chem}} \geq T_{\mathrm{kin}}$ is expected. Values of the statistical parameters at the chemical freeze-out are determined from fits to particle yield ratios, whereas corresponding values at the kinetic freeze-out are fitted to the spectra of hadrons. From here forward, statistical parameters at the kinetic freeze-out mean their values fitted to the spectra. $T_{\mathrm{chem}} \sim 150$–$170\,\mathrm{MeV}$ is estimated at highest heavy-ion reaction energy [3–13]. Additionally, fits done for various centrality classes have revealed that $T_{\mathrm{chem}}$ is almost independent of centrality [4, 6, 8–10]. On the contrary, the temperature at the kinetic freeze-out depends on the centrality and is substantially lower. From the most central to the peripheral bin it changes as follows: $T_{\mathrm{kin}} = 121$–$161\,\mathrm{MeV}$ for PHENIX at $\sqrt{s_{\mathrm{NN}}} = 130\,\mathrm{GeV}$ [14], $T_{\mathrm{kin}} = 111$–$147\,\mathrm{MeV}$ for PHENIX at

$\sqrt{s_{\rm NN}} = 200\,{\rm GeV}$ [15], $T_{\rm kin} = 89$–$129\,{\rm MeV}$ for STAR at $\sqrt{s_{\rm NN}} = 200\,{\rm GeV}$ [9] and $T_{\rm kin} = 110$–$115\,{\rm MeV}$ for BRAHMS at $\sqrt{s_{\rm NN}} = 200$ GeV [16]. For the PHOBOS data at $\sqrt{s_{\rm NN}} = 62.4\,{\rm GeV}$ $T_{\rm kin} = 103, 102, 101\,{\rm MeV}$ for the central, mid-peripheral and peripheral bin, respectively [17]. However, the aforementioned estimates of $T_{\rm kin}$ have been done within the very simplified hydrodynamic model, *i.e.* the blast-wave model [18].

The main difference between fitting the statistical parameters at the chemical freeze-out and at the thermal freeze-out is that the first procedure is independent of a pattern of expansion. Thus, assuming boost invariance and that statistical parameters are constant on a freeze-out hypersurface one has

$$\frac{(dN_i/dy)_{y=0}}{(dN_j/dy)_{y=0}} = \frac{N_i}{N_j} = \frac{n_i}{n_j}\,, \tag{1}$$

where the last equality follows from the factorization of the volume of the system (for more details see [19–21]) and the density of particle species $i$ reads

$$n_i(T,\mu_{\rm B}) = n_i^{\rm primordial}(T,\mu_{\rm B}) + \sum_a \varrho\,(i,a)\; n_a^{\rm primordial}(T,\mu_{\rm B})\,, \tag{2}$$

where $n_a^{\rm primordial}(T,\mu_{\rm B})$ is the thermal density of the $a$th particle species at the freeze-out, $\varrho(i,a)$ is the final number of particles of species $i$ which can be received from all possible simple or sequential decays of particle $a$ and the sum is over all species of resonances included in the hadron gas. This means that values of the statistical parameters at the chemical freeze-out do not depend on the assumed model of expansion. Therefore, fitting measured ratios cannot distinguish between the blast wave model and the present model. The only sources of valuable information about the pattern of expansion are measured spectra.

In this paper, it will be shown that the behavior of $T_{\rm kin}$ is model dependent and within a different hypersurface and with complete treatment of resonance decays different conclusions about statistical parameters at the kinetic freeze-out can be obtained. Namely, the statistical parameters at the kinetic freeze-out are roughly centrality independent and their values are close to the corresponding values at the chemical freeze-out.

## 2. Foundations of the model

The model applied here is inspired by the single-freeze-out model of Refs [22, 23], but its main assumption about the simultaneous occurrence of chemical and thermal freeze-outs *is not postulated*. The assumptions of the present model are as follows. A noninteracting gas of stable hadrons and resonances at chemical and thermal equilibrium appears at the latter stages

of a heavy-ion collision. The gas cools and expands, and after reaching the freeze-out point it ceases. The conditions for the freeze-out are expressed by values of two independent thermal parameters: $T$ and $\mu_{\rm B}$. The strangeness chemical potential $\mu_{\rm S}$ is determined from the requirement that the overall strangeness equals zero. All confirmed resonances up to a mass of 2 GeV from the Particle Data Tables [24], together with stable hadrons, are constituents of the gas. The freeze-out hypersurface is defined by the equation

$$\tau = \sqrt{t^2 - r_x^2 - r_y^2 - r_z^2} = \text{const}\,. \tag{3}$$

with the additional condition

$$r = \sqrt{r_x^2 + r_y^2} < \rho_{\max} \tag{4}$$

which makes the transverse size of the system finite. $\tau$ and $\rho_{\max}$ constitute two geometric parameters of the model.

The four-velocity of an element of the freeze-out hypersurface is proportional to its coordinate

$$u^\mu = \frac{x^\mu}{\tau} = \frac{t}{\tau}\,\left(1, \frac{r_x}{t}, \frac{r_y}{t}, \frac{r_z}{t}\right)\,. \tag{5}$$

The shape of the hypersurface defined by Eqs (3), (4) and the above form of the flow imply that the model is longitudinally boost-invariant and cylindrically symmetric. The last feature is fulfilled strictly only in the case of a central collision, but experimental spectra are averaged over the azimuthal angle, which means that they look as if they were uniform in this angle. In the view of Eq. (5), $\tau$ given by Eq. (3) is the usual proper time of the fluid element. Thus in this model the freeze-out takes place at the same moment of time in the local rest frame of a fluid element. In the c.m.s. of the colliding nuclei this means that the farther particles are from the center of the collision the later they freeze out. For the 1+1 dimensional Bjorken model [25] this is the direct conclusion from the form of its solution: all thermodynamical quantities depend only on a local proper time $\tau = \sqrt{t^2 - z^2}$, so if one assumes that the freeze-out takes place at a given temperature, $T_{\rm f.o.}$, it means that it happens at one moment of the proper time. The same is true for a spherically symmetric expansion in 1+3 dimensions at sufficiently long times [26]. Note, that in that case the freeze-out hypersurface has also the shape given by Eq. (3). The form of the four-velocity, as implied by Eq. (5), determines the three-velocity, $\vec{v} = \vec{r}/t$. This is the so-called *scaling solution*, which is the exact solution for the Bjorken model [25]. In 1+3 dimensions it was shown that for a spherically symmetric expansion the scaling solution might develop if the sound velocity squared satisfies $c_s^2 < 0.2$ [26].

For boost-invariant, cylindrically symmetric systems recent results of Ref. [27] indicate that the scaling solution can develop in 130 and 200 GeV Au–Au collisions within times 7–15 fm. This is roughly the scale of the freeze-out initializing time predicted in this analysis for central and mid-central bins (see Table I).

The following parameterization of the hypersurface is chosen:

$$\begin{aligned} t &= \tau \cosh\alpha_{\parallel} \cosh\alpha_{\perp}\,, \qquad & r_x &= \tau \sinh\alpha_{\perp} \cos\phi\,, \\ r_y &= \tau \sinh\alpha_{\perp} \sin\phi\,, & r_z &= \tau \sinh\alpha_{\parallel} \cosh\alpha_{\perp}\,, \end{aligned} \tag{6}$$

where $\alpha_{\parallel}$ is the rapidity of the element, $\alpha_{\parallel} = \tanh^{-1}(r_z/t)$, and $\alpha_{\perp}$ controls the transverse radius $r = \tau \sinh\alpha_{\perp}$.

The maximum transverse-flow parameter (or the surface velocity) at the central slice is given by

$$\beta_{\perp}^{\max} = \frac{\rho_{\max}}{\sqrt{\tau^2 + \rho_{\max}^2}} = \frac{\rho_{\max}/\tau}{\sqrt{1 + (\rho_{\max}/\tau)^2}}\,. \tag{7}$$

The invariant distribution of the measured particles of species $i$ has the form [22, 23]

$$\frac{dN_i}{d^2p_{\mathrm{T}}\,dy} = \int p^{\mu} d\sigma_{\mu}\; f_i(p\cdot u)\,, \tag{8}$$

where $d\sigma_{\mu}$ is the normal vector on a freeze-out hypersurface, $p\cdot u = p^{\mu}u_{\mu}$ , $u_{\mu}$ is the four-velocity of a fluid element and $f_i$ is the final momentum distribution of the particle in question. The final distribution means here that $f_i$ is the sum of primordial and simple and sequential decay contributions to the particle distribution. The primordial part of $f_i$ is given by a Bose–Einstein or a Fermi–Dirac distribution at the freeze-out. A decay contribution is a one-dimensional or multidimensional integral of the momentum distribution of a decaying resonance (the exact formulae are obtained from the elementary kinematics of a many-body decay or the superposition of such decays, for details see [19] and the Appendix in [28]). The resonance is a constituent of the hadron gas and its distribution is also given by the Bose–Einstein (Fermi–Dirac) distribution function. Therefore, the final distribution $f_i$ depends explicitly on $T$ and $\mu_{\mathrm{B}}$.

With the use of Eqs (5) and (6), the invariant distribution (8) takes the following form:

$$\frac{dN_i}{d^2p_{\mathrm{T}}\,dy} = \tau^3 \int\limits_{-\infty}^{+\infty} d\alpha_{\parallel} \int\limits_{0}^{\rho_{\max}/\tau} \sinh\alpha_{\perp} d(\sinh\alpha_{\perp}) \int\limits_{0}^{2\pi} d\xi\; p\cdot u\; f_i(p\cdot u)\,, \tag{9}$$

where

$$p\cdot u = m_{\mathrm{T}} \cosh(\alpha_{\parallel} - y) \cosh\alpha_{\perp} - p_{\mathrm{T}} \cos\xi \sinh\alpha_{\perp}\,. \tag{10}$$

The model has four parameters, the two thermal parameters, the temperature $T$ and the baryon number chemical potential $\mu_{\rm B}$, and the two geometric parameters, $\tau$ and $\rho_{\rm max}$. It should be stressed that now all parameters of the model are fitted simultaneously, opposite to the case of Refs [22, 23] where the determination proceeded in two steps. First, statistical parameters $T$ and $\mu_{\rm B}$ were fitted with the use of the experimental ratios of hadron multiplicities at midrapidity. Then geometric parameters were determined from fits to the transverse-momentum spectra. Therefore, the assumption that the chemical freeze-out happens simultaneously with the kinetic freeze-out (the single freeze-out) was crucial in that approach. Now all parameters are fitted to the spectra, so the aforementioned assumption is not necessary and values of statistical parameters have the meaning of the values at the kinetic freeze-out.

With the use of Eq. (9) the measured transverse-momentum spectra of $\pi^{\pm}$, $K^{\pm}$, $p$ and $\bar{p}$ [9, 14, 16, 17, 29] can be fitted to determine values of the parameters of the model (data points with $p_{\rm T} > 3$ GeV have been excluded). Fits are performed with the help of the $\chi^2$ method. For the $k$th measured quantity $R_k^{\rm exp}$ and its theoretical equivalent $R_k^{\rm th}(\alpha_1, ..., \alpha_l)$, which depends on $l$ parameters $\alpha_1, ..., \alpha_l$, the $\chi^2$ function is defined as

$$\chi^2(\alpha_1, ..., \alpha_l) = \sum_{k=1}^{n} \frac{\left(R_k^{\rm exp} - R_k^{\rm th}(\alpha_1, ..., \alpha_l)\right)^2}{\sigma_k^2}\,, \tag{11}$$

where $\sigma_k$ is the error of the $k$th measurement and $n$ is the total number of data points. The fitted (optimum) values of parameters mean the values at which $\chi^2$ has a minimum.

## 3. Results

The fitted results for $T_{\rm kin}$, $\mu_{\rm B}$, $\rho_{\rm max}$ and $\tau$ are collected in Table I together with values of the surface velocity $\beta_{\perp}^{\rm max}$ and values of $\chi^2$/NDF for each centrality class additionally characterized by the number of participants $N_{\rm part}$. Errors are expressed by one standard deviation ($1\sigma$). Note that except the most peripheral bins of the PHENIX measurements all fits are statistically significant. That these new higher values of temperature (higher in comparison with the blast-wave fit values) are at minima is shown in Fig. 1 in an example of the temperature dependence of $\chi^2$ for the PHENIX most central bin at $\sqrt{s_{\rm NN}} = 200$ GeV. The simulation of the dependence was done within the same procedure as in the original single-freeze-out model, with the overall fixed value of $\mu_{\rm B} = 27.5$ MeV (the average of values from [8, 12]) and the temperature fixed at each point and taken from the range 120–180 MeV with the 1 or 2 MeV step. Then two geometric parameters were fitted and $\chi^2$ at their optimum values was put into the figure.

TABLE I

Values of the statistical and geometric parameters of the model for various centrality bins fitted with the use of the RHIC final data for the $p_{\mathrm{T}}$ spectra of identified charged hadrons [9, 14, 16, 29]. All data are at midrapidity, except the PHOBOS case (first three rows) where data are at $y=0.8$ [17].

| Au–Au collision case | Centrality [%] | $N_{\mathrm{part}}$ | $T_{\mathrm{kin}}$ [MeV] | $\mu_{\mathrm{B}}$ [MeV] | $\rho_{\max}$ [fm] | $\tau$ [fm] | $\beta_{\perp}^{\max}$ | $\chi^2$/NDF | NDF |
|---|---|---|---|---|---|---|---|---|---|
| PHOBOS at | 0–15 | 294.0 | 148.52±1.15 | 72.60±3.81 | 7.84±0.19 | 8.35±0.14 | 0.684±0.006 | 0.995 | 72 |
| $\sqrt{s_{\mathrm{NN}}} = 62.4$ GeV | 15–30 | 175.0 | 149.64±1.42 | 69.47±4.13 | 6.23±0.19 | 7.20±0.17 | 0.654±0.007 | 0.43 | 72 |
| | 30–50 | 88.0 | 151.29±1.70 | 67.15±4.47 | 4.60±0.18 | 6.05±0.18 | 0.605±0.009 | 0.20 | 71 |
| | 0– 5 | 347.7 | 166.74±3.96 | 35.06±8.97 | 6.31±0.41 | 8.08±0.44 | 0.616±0.014 | 0.53 | 78 |
| PHENIX at | 5–15 | 271.3 | 161.70±3.21 | 43.14±7.77 | 6.34±0.35 | 7.57±0.34 | 0.642±0.012 | 0.46 | 78 |
| $\sqrt{s_{\mathrm{NN}}} = 130$ GeV | 15–30 | 180.2 | 162.33±3.29 | 38.52±7.75 | 5.32±0.29 | 6.54±0.29 | 0.631±0.012 | 0.50 | 78 |
| | 30–60 | 78.5 | 162.25±3.46 | 31.80±7.87 | 3.77±0.23 | 4.95±0.23 | 0.606±0.015 | 0.75 | 78 |
| | 60–92 | 14.3 | 159.46±6.85 | 37.05±16.09 | 1.87±0.27 | 3.26±0.27 | 0.496±0.043 | 1.37 | 42 |
| | 0– 5 | 351.4 | 150.07±1.34 | 24.10±3.66 | 9.28±0.21 | 9.48±0.19 | 0.699±0.004 | 0.69 | 122 |
| PHENIX at | 5–10 | 299.0 | 150.18±1.35 | 23.48±3.65 | 8.75±0.20 | 8.80±0.18 | 0.705±0.004 | 0.50 | 122 |
| $\sqrt{s_{\mathrm{NN}}} = 200$ GeV | 10–15 | 253.9 | 150.16±1.35 | 22.75±3.65 | 8.25±0.19 | 8.20±0.17 | 0.709±0.004 | 0.37 | 122 |
| | 15–20 | 215.3 | 150.00±1.36 | 22.38±3.65 | 7.80±0.18 | 7.69±0.16 | 0.712±0.004 | 0.37 | 122 |
| | 20–30 | 166.6 | 149.59±1.31 | 24.03±3.47 | 7.13±0.16 | 6.96±0.14 | 0.716±0.004 | 0.45 | 122 |
| | 30–40 | 114.2 | 149.79±1.36 | 23.78±3.56 | 6.14±0.14 | 6.03±0.12 | 0.713±0.004 | 0.66 | 122 |
| | 40–50 | 74.4 | 148.53±1.40 | 22.52±3.71 | 5.28±0.13 | 5.27±0.11 | 0.708±0.005 | 0.89 | 122 |
| | 50–60 | 45.5 | 147.75±1.51 | 22.02±4.03 | 4.38±0.12 | 4.55±0.10 | 0.694±0.005 | 0.96 | 122 |
| | 60–70 | 25.7 | 144.57±1.65 | 21.63±4.56 | 3.63±0.11 | 3.91±0.09 | 0.680±0.006 | 1.12 | 122 |
| | 70–80 | 13.4 | 141.77±1.98 | 24.13±5.68 | 2.84±0.10 | 3.22±0.09 | 0.662±0.008 | 1.23 | 122 |
| | 80–92 | 6.3 | 140.62±2.46 | 14.29±7.12 | 2.24±0.10 | 2.77±0.09 | 0.630±0.011 | 1.13 | 122 |
| | 0– 5 | 352.0 | 159.99±1.19 | 24.00±2.17 | 9.22±0.31 | 7.13±0.19 | 0.791±0.006 | 0.30 | 71 |
| STAR at | 5–10 | 299.0 | 160.58±1.16 | 24.97±2.17 | 8.34±0.28 | 6.75±0.18 | 0.777±0.006 | 0.27 | 71 |
| $\sqrt{s_{\mathrm{NN}}} = 200$ GeV | 10–20 | 234.0 | 161.20±1.14 | 22.91±2.15 | 7.45±0.24 | 6.17±0.16 | 0.770±0.006 | 0.22 | 73 |
| | 20–30 | 166.0 | 162.27±1.12 | 23.05±2.17 | 6.31±0.20 | 5.60±0.14 | 0.748±0.007 | 0.25 | 75 |
| | 30–40 | 115.0 | 161.97±1.08 | 20.43±2.17 | 5.38±0.17 | 5.15±0.12 | 0.722±0.007 | 0.19 | 75 |
| | 40–50 | 76.0 | 162.97±1.08 | 21.01±2.21 | 4.46±0.14 | 4.64±0.11 | 0.693±0.008 | 0.13 | 75 |
| | 50–60 | 47.0 | 163.41±1.07 | 18.75±2.25 | 3.67±0.12 | 4.13±0.10 | 0.664±0.008 | 0.13 | 75 |
| | 60–70 | 27.0 | 162.39±1.06 | 16.47±2.31 | 2.95±0.10 | 3.79±0.09 | 0.614±0.010 | 0.26 | 75 |
| | 70–80 | 14.0 | 163.70±1.15 | 15.84±2.50 | 2.22±0.09 | 3.16±0.08 | 0.574±0.012 | 0.61 | 75 |
| | 0–10 | 328.0 | 150.60±1.39 | 23.07±3.51 | 9.26±0.25 | 8.65±0.21 | 0.731±0.004 | 0.43 | 114 |
| BRAHMS at | 10–20 | 239.0 | 151.38±1.48 | 26.53±3.72 | 8.07±0.23 | 7.68±0.19 | 0.724±0.005 | 0.42 | 114 |
| $\sqrt{s_{\mathrm{NN}}} = 200$ GeV | 20–40 | 140.0 | 149.43±1.54 | 25.92±3.98 | 7.00±0.21 | 6.73±0.17 | 0.721±0.005 | 0.26 | 112 |
| | 40–60 | 62.0 | 148.36±2.02 | 26.69±5.21 | 5.02±0.20 | 5.38±0.17 | 0.683±0.008 | 0.52 | 112 |

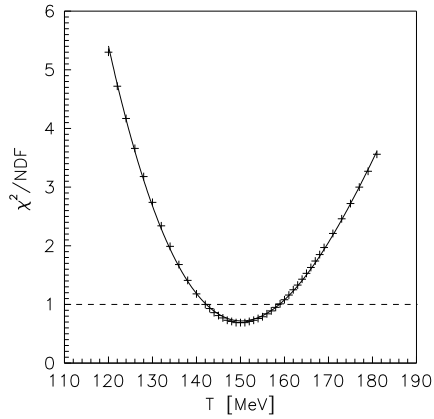


Fig. 1. Simulation of the temperature dependence of $\chi^2$/NDF for PHENIX at $\sqrt{s_{\rm NN}} = 200$ GeV and the 0–5% centrality class. Solid line is the polynomial 3 best fit.

Coming back to the results of simultaneous fits of all four parameters, some $1\sigma$ and $2\sigma$ contours are presented in Figs 2 and 3. These contours are done in $T_{\rm kin}$ and $\beta_\perp^{\rm max}$ planes to make them comparable with the blast-wave results. But since the parameter space is four dimensional, the $n$-sigma contour is in fact the 3-dimensional ellipsoid embedded in this space, so it can be presented only by means of its projections on some planes. Contours presented in Figs 2 and 3 are such projections onto $T_{\rm kin}$ and $\beta_\perp^{\rm max}$ planes chosen at some fixed $\mu_{\rm B}$ and $\tau$, namely at their optimum values $\mu_{\rm B,opt}$ and $\tau_{\rm opt}$, Fig. 2, and at $\mu_{\rm B} = \mu_{\rm B,opt} \pm 0.5\sigma_\mu$ and $\tau = \tau_{\rm opt} \pm 0.5\sigma_\tau$, Fig. 3. Note that in Fig. 3 black dots denote the projections of the points of optimum values

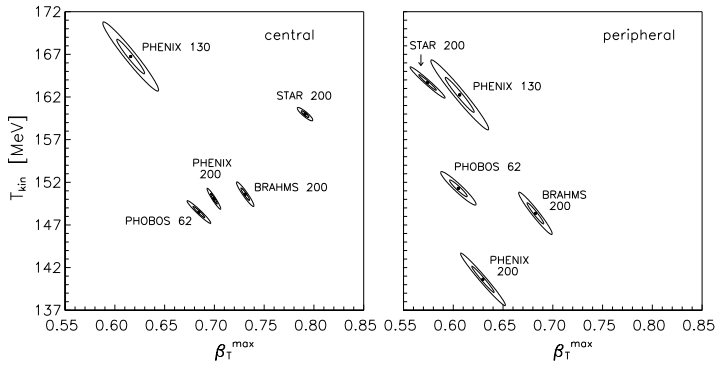


Fig. 2. The $\chi^2$ contours ($1\sigma$ and $2\sigma$) in the parameter plane $T_{\rm kin}$ and $\beta_\perp^{\rm max}$ fixed by taking $\mu_{\rm B}$ and $\tau$ at their optimum values. In the right panel the PHENIX case at $\sqrt{s_{\rm NN}} = 130$ GeV is represented by the second from the most peripheral bin, see text for explanations. Dots denote the optimum values of $T_{\rm kin}$ and $\beta_\perp^{\rm max}$.

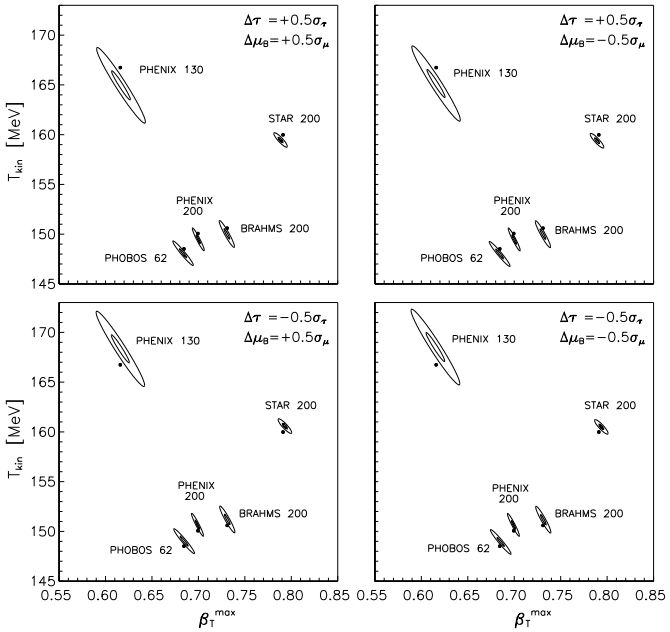


Fig. 3. The $\chi^2$ contours ($1\sigma$ and $2\sigma$) in the parameter planes $T_{\rm kin}$ and $\beta_\perp^{\rm max}$ fixed by taking $\mu_{\rm B}$ and $\tau$ at $\pm 0.5\sigma$ from their optimum values, $\triangle\tau = \tau - \tau_{\rm opt}$, $\triangle\mu_{\rm B} = \mu_{\rm B} - \mu_{\rm B,opt}$. All cases represent the most central classes. Dots denote the projections of the points of optimum values of all parameters onto the appropriate plane $T_{\rm kin} - \beta_\perp^{\rm max}$.

of all parameters onto the appropriate plane $T_{\rm kin}$–$\beta_\perp^{\rm max}$, this is the reason why they are outside the contours. In the right panel of Fig. 2, all examples are for most peripheral bins, except the PHENIX case at $\sqrt{s_{\rm NN}} = 130\,{\rm GeV}$ which is for the second from the most peripheral class. This is because errors in the case of the most peripheral bin of the PHENIX measurements at $\sqrt{s_{\rm NN}} = 130\,{\rm GeV}$ are substantially greater (see Table I), which results in too big extension of $1\sigma$ and $2\sigma$ contours ($\sim 3$ times bigger than in the second from the most peripheral bin). This fact together with $\chi^2/{\rm NDF}$ much higher than 1 does not enable to determine firm optimum values of $T_{\rm kin}$ and $\beta_\perp^{\rm max}$ in this case. Generally, $\chi^2$ is flatter in the vicinity of the optimum points for PHENIX at $\sqrt{s_{\rm NN}} = 130$ GeV, as one can notice from Figs 2 and 3. This is also expressed by $\sim 2$ times greater errors of the fitted values in this case. For other experiments $1\sigma$ and $2\sigma$ contours are relatively small. Their sizes do not change visibly from most central to mid-central bins and then increase gradually up to the sizes of the contours for most peripheral bins (in fact this behavior reflects the behavior of the corresponding errors, *cf.* Table I).

The feeding from weak decays is treated in the same way as experimental groups do, except the STAR case. So, for the PHENIX measurements at $\sqrt{s_{\rm NN}} = 200$ GeV protons (antiprotons) from $\Lambda$ ($\bar{\Lambda}$) decays are excluded. In the PHOBOS case protons (antiprotons) from $\Lambda$ and $\Sigma^+$ ($\bar{\Lambda}$ and $\bar{\Sigma}^-$) decays are not counted. As far as STAR is considered, this collaboration has corrected its pion spectra for weak decays [9]. However, STAR also claims there that when the full feeding from weak decays is taken into account the single-freeze-out model with all the resonances can fit the spectra but with higher $\chi^2$/NDF. Therefore, to check this statement all weak decays are included in the STAR data analysis.

Results for $T_{\rm kin}$ and $\mu_{\rm B}$ are also depicted as functions of $N_{\rm part}$ in Fig 4 (left) and (right), respectively. It is clearly seen that both $T_{\rm kin}$ and $\mu_{\rm B}$ are almost independent of the collision centrality, only for peripheral bins some dependence can be observed. Additionally, their values are very close to the values at the chemical freeze-out. Namely, $T_{\rm chem} = 165$–$169$ MeV and $\mu_{\rm B} = 33$–$38$ MeV from the peripheral to most central bin at $\sqrt{s_{\rm NN}} = 130$ GeV was found in Ref. [6], $T_{\rm chem} \approx 155$ MeV and $\mu_{\rm B} \approx 26$ MeV independent of the centrality for PHENIX at $\sqrt{s_{\rm NN}} = 200$ GeV in Ref. [8] and $T_{\rm chem} \approx 160$ MeV independent of the centrality and $\mu_{\rm B} = 15$–$24$ MeV from the peripheral to most central bin for STAR at $\sqrt{s_{\rm NN}} = 200$ GeV in Refs [9–11].

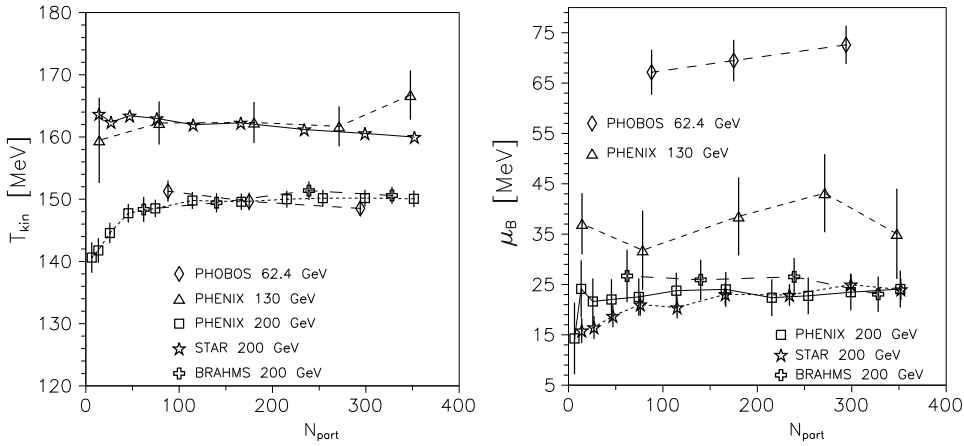


Fig. 4. Centrality dependence of the kinetic freeze-out temperature (left) and of the baryon number chemical potential (right), for the RHIC measurements at $\sqrt{s_{\rm NN}} =$ 62.4, 130 and 200 GeV. The lines connect the results and are a guide.

In Figs 5–9 measured and predicted spectra of identified hadrons are presented for some collisions at RHIC. In Fig. 5 the case of PHOBOS at $\sqrt{s_{\rm NN}} = 62.4$ GeV is dealt with. The way the data and results are depicted is suggested by the PHOBOS analysis [17] (see Fig. 7 there). The lines are predictions of the present model done with the use of fitted parameters tabulated in Table I. But fits were done within intermediate ranges of $p_{\rm T}$,

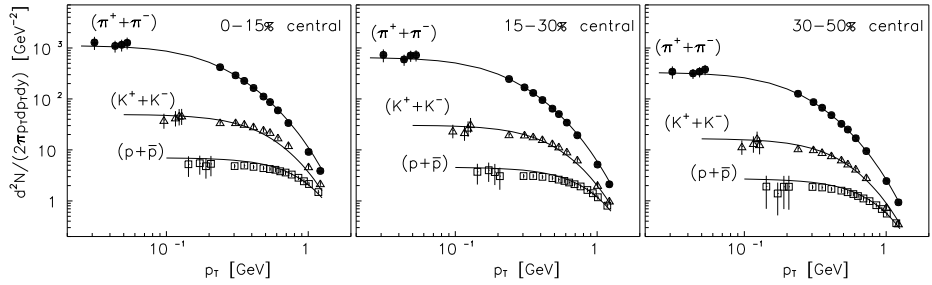


Fig. 5. Invariant yields as a function of $p_{\rm T}$ in Au+Au collisions at $\sqrt{s_{\rm NN}} = 62.4$ GeV. Lines are predictions of the present model and symbols are PHOBOS data [17].

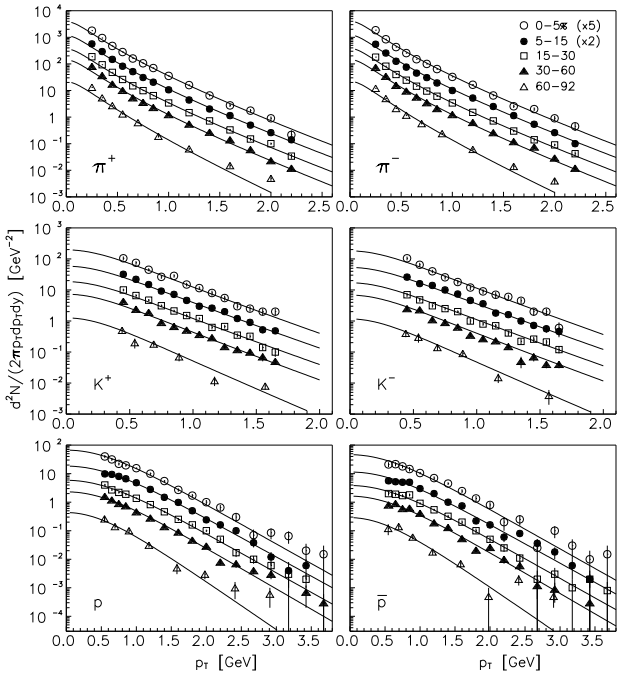


Fig. 6. Invariant yields as a function of $p_{\rm T}$ in Au+Au collisions at $\sqrt{s_{\rm NN}} = 130$ GeV. Lines are predictions of the present model and symbols are PHENIX data [14]. For clarity, the data points are scaled vertically for two bins as quoted in the figure.

that is in the ranges where single charged hadron data exist. Then predictions were made for sums of negatively and positively charged hadrons of the same kind but in the whole accessible ranges, namely ranges extended to the very low $p_{\mathrm{T}}$ where separate data on the summed yields exist. As one can see from Fig. 5 predictions of the model agree very well with the data, only slight overestimation of protons and antiprotons can be observed but for the very low $p_{\mathrm{T}}$ region results agree within errors. Predictions of the blast-wave model also agree with the data (*cf.* Fig. 7 in [17]), but opposite to the present analysis, they underestimate pion yields and correctly estimate proton and antiproton yields at very low $p_{\mathrm{T}}$. For the collisions at $\sqrt{s_{\mathrm{NN}}} = 130\,\mathrm{GeV}$, Fig. 6, predictions for pion and kaon spectra agree very well with the PHENIX data, whereas for protons and antiprotons the agreement holds up to $p_{\mathrm{T}} \approx 2.5$ GeV. Similar results were obtained within the blast-wave model (*cf.* Fig. 19 in [14]). In Figs 7–9 results and data are presented for the PHENIX measurements at $\sqrt{s_{\mathrm{NN}}} = 200$ GeV. Predictions for pions, Fig. 7, agree very well with the data practically in the whole $p_{\mathrm{T}}$ range for the first five bins from the top, for the next bins the predictions start to miss the data at $p_{\mathrm{T}} \approx 2.5$ GeV and this value is decreasing with the centrality to $p_{\mathrm{T}} \approx 2$ GeV for the most peripheral bin. Kaons are reproduced very well in the whole range of $p_{\mathrm{T}}$ and for all centralities, as one can see in Fig. 8. Protons and antiprotons agree very well up to $p_{\mathrm{T}} \approx 3.3$ GeV for first nine bins from the top, for the two last peripheral bins the agreement is lost at $p_{\mathrm{T}} \approx 2.5$ GeV, as it can be seen in Fig. 9.

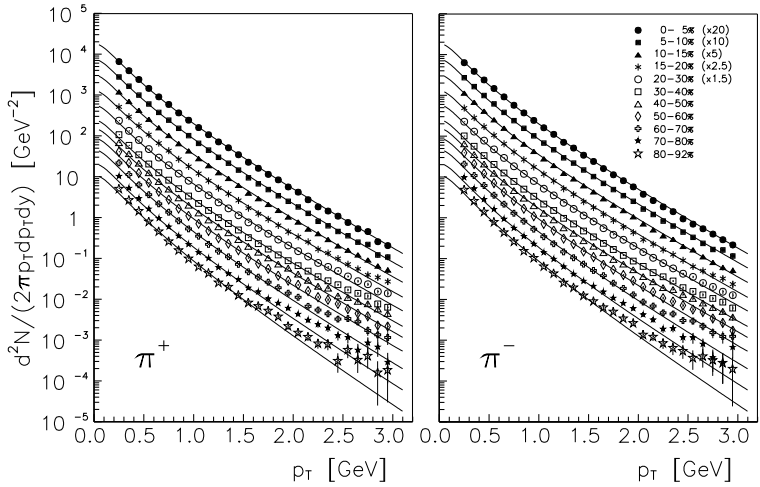


Fig. 7. Invariant yields of $\pi^+$ (left) and $\pi^-$ (right) as a function of $p_{\mathrm{T}}$ in Au+Au collisions at $\sqrt{s_{\mathrm{NN}}} = 200\,\mathrm{GeV}$. Lines are predictions of the present model and symbols are PHENIX data [29]. For clarity, the data points are scaled vertically for five bins as quoted in the figure.

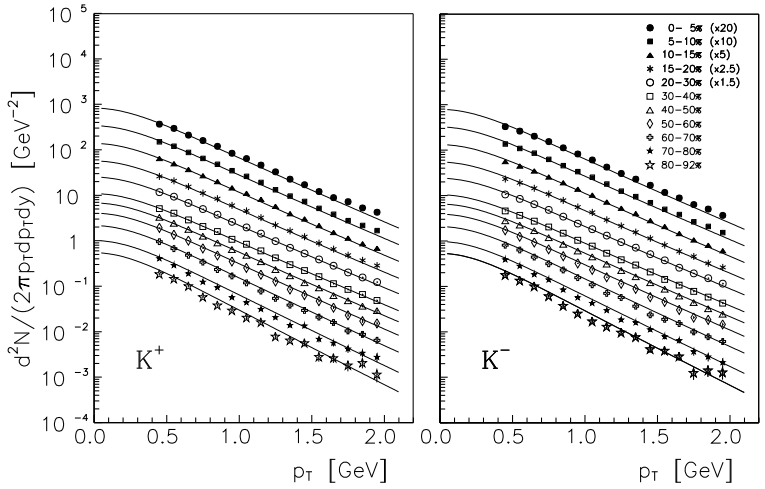


Fig. 8. Invariant yields of $K^+$ (left) and $K^-$ (right) as a function of $p_{\mathrm{T}}$ in Au+Au collisions at $\sqrt{s_{\mathrm{NN}}} = 200\,\mathrm{GeV}$. Lines are predictions of the present model and symbols are PHENIX data [29]. For clarity, the data points are scaled vertically for five bins as quoted in the figure.

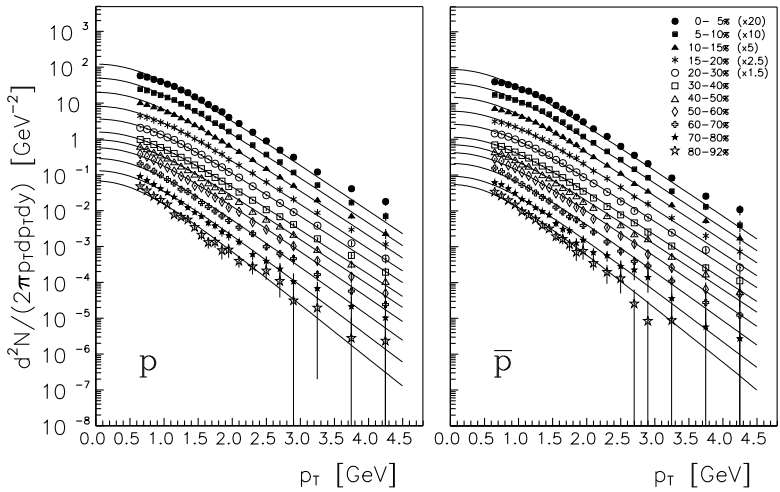


Fig. 9. Invariant yields of protons (left) and anti-protons (right) as a function of $p_{\mathrm{T}}$ in Au+Au collisions at $\sqrt{s_{\mathrm{NN}}} = 200\,\mathrm{GeV}$. Lines are predictions of the present model and symbols are PHENIX data [29]. For clarity, the data points are scaled vertically for five bins as quoted in the figure.

A simple test of the model can be performed with the use of the spectra of $\Omega$ hyperon. This is because $\Omega$ has only the thermal contribution to the invariant distribution, Eq. (9). Such a test has been done for the

blast-wave model [10] and for the single-freeze-out model [12], but in both cases the comparison was done with preliminary data. Present results together with the STAR data for $\Omega^- + \bar{\Omega}^+$ production at $\sqrt{s_{\rm NN}} = 200\,{\rm GeV}$ are shown in Fig. 10. Values of parameters for 20–40 % and 40–60 % centrality bins explored by STAR in $\Omega$ measurements are the averages of the values from Table I for bins which added percent coverage equals 20–40 % and 40–60 %, respectively. One can see that predictions based on fits to PHENIX spectra agree well with the data. Predictions based on fits to STAR spectra agree only qualitatively, they have higher normalization. Also for the 0–5 % bin the slope differs. Blast-wave model predictions for $\Omega^- + \bar{\Omega}^+$ spectrum for the 0–5 % bin of the preliminary STAR data were done in Ref. [10], but they do not agree with the data neither in normalization nor in a slope. The probable reason for the worse agreement of the STAR data based predictions in the present model, Fig. 10, is that STAR spectra of identified stable hadrons are measured in narrower ranges of $p_{\rm T}$ than PHENIX ones, *i.e.* $p_{\rm T} \in [0.2, 1.2]\,{\rm GeV}/c$ approximately for STAR [9] whereas for PHENIX $p_{\rm T} \in [0.25, 2.95]\,{\rm GeV}/c$ (pions), $p_{\rm T} \in [0.55, 1.95]\,{\rm GeV}/c$ (kaons) and $p_{\rm T} \in [0.65, 4.25]\,{\rm GeV}/c$ [(anti)protons] [29]. And the STAR measurement of $\Omega^- + \bar{\Omega}^+$ is done within the range $p_{\rm T} \in [1.25, 4]\,{\rm GeV}/c$, practically outside the STAR range of $p_{\rm T}$ of identified stable hadrons but covering the great part of PHENIX $p_{\rm T}$ ranges. Also they differ in common ranges of $p_{\rm T}$, namely STAR spectra are placed slightly above the corresponding PHENIX spectra and in the case of pions have different slopes (it has been checked carefully for the common 0–5 % bin after conversion of STAR spectra from

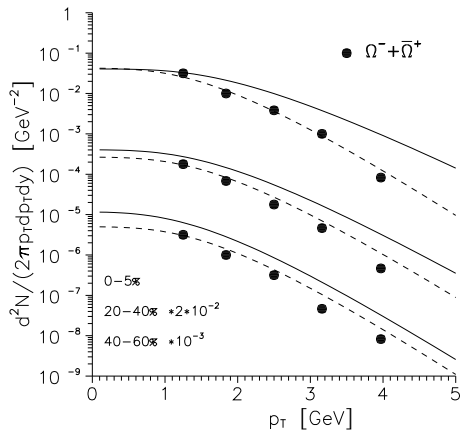


Fig. 10. Transverse momentum distributions of $\Omega^- + \bar{\Omega}^+$ for $\mid y \mid < 0.75$ in Au–Au collisions at $\sqrt{s_{\rm NN}} = 200\,{\rm GeV}$. Data are from [31] (STAR) scaled for clarity, (statistical) errors are of the size of symbols. Lines denote model predictions: solid based on fits to the STAR spectra, dashed based on fits to the PHENIX spectra.

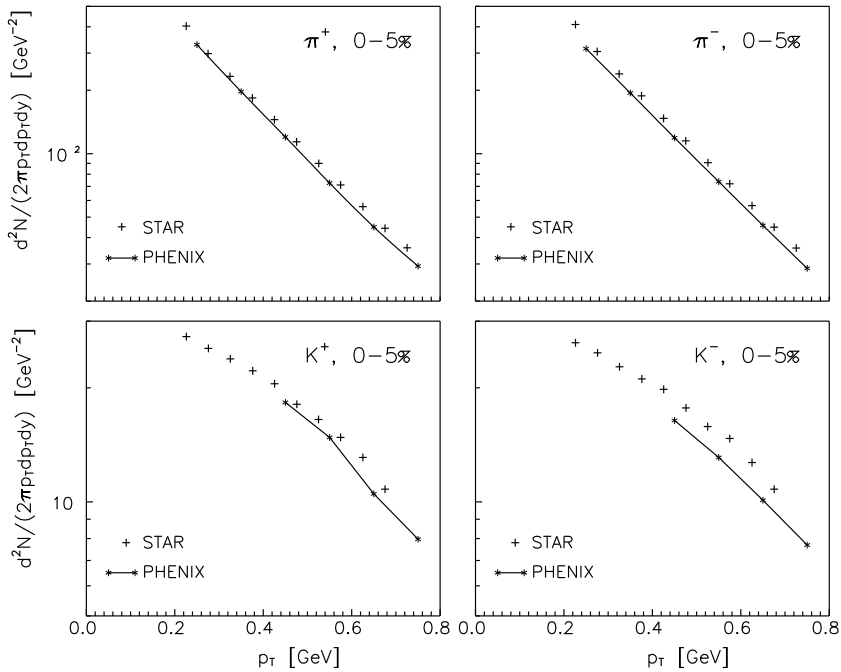


Fig. 11. Comparison of $\pi^+$, $\pi^-$, $K^+$ and $K^-$ spectra measured by STAR and PHENIX for the 0–5 % centrality bin at $\sqrt{s_{\rm NN}} = 200\,\text{GeV}$. All STAR data points are depicted, whereas PHENIX data ranges are cut from the right-hand side (in fact they extend to $p_{\rm T} = 2.95\,\text{GeV}$ for pions and $p_{\rm T} = 1.95\,\text{GeV}$ for kaons).

$m_{\rm T}$–$m_i$ to $p_{\rm T}$, see Fig. 11). Actually, the difference in pion spectra is even greater than what can be seen in Fig. 11, because the STAR pion spectra are corrected for weak decays [9]. Proton and antiproton spectra are not compared, since the PHENIX subtracted protons (antiprotons) from $\Lambda$ ($\bar{\Lambda}$) decays, so by definition the STAR proton (antiproton) spectra are above the PHENIX ones. Also that the STAR minimizations have lower $\chi^2$/NDF than PHENIX ones is probably because it is much easier to fit over a narrower range of $p_{\rm T}$. Discrepancies between STAR and PHENIX spectra explain why the optimum values of parameters are different for these collaborations. These discrepancies could be caused by the different detectors used by the aforementioned collaborations. The PHENIX uses a spectrometer, which consists of drift chamber (DC), pad chamber (PC) and time-of-flight (TOF) [29], whereas the STAR uses time projection chamber (TPC) [9]. The TPC is better in measurements of resonances but the PHENIX spectrometer measures spectra of identified particles more precisely [8,32]. This might also help to understand why $\Omega^- + \bar{\Omega}^+$ measured spectra (an example of the

STAR data on resonance production) are well reproduced in the model with the use of the parameters fitted to the PHENIX data on identified stable hadrons (in addition to the earlier argument based on the compatibility of $p_{\mathrm{T}}$ ranges).

## 4. Discussion and conclusions

Before the final conclusion one result of Ref. [2] should be commented. In [2] a hydrodynamical model supplemented with the dynamical freeze-out criterium [33–35]

$$\frac{1}{\tau_{\mathrm{scatt}}} = \xi \, \frac{1}{\tau_{\mathrm{exp}}} = \xi \, \partial_\mu u^\mu \,, \tag{12}$$

where $1/\tau_{\mathrm{scatt}}$ is the local scattering rate and $1/\tau_{\mathrm{exp}}$ is the local expansion rate and the parameter $\xi \sim 1$ was successfully used to explain the centrality dependence and the temperature range of $T_{\mathrm{kin}}$ determined from the blast-wave fits to the STAR data at $\sqrt{s_{\mathrm{NN}}} = 200\,\mathrm{GeV}$ [9]. To obtain the $T_{\mathrm{kin}}$ range comparable with the STAR results, $T_{\mathrm{kin}} \simeq 90$–$130\,\mathrm{MeV}$, the appropriate adjustment of the parameter $\xi$ was done, $\xi = 0.295$. Then, the range $T_{\mathrm{kin}} \simeq 105$–$135\,\mathrm{MeV}$ was obtained in [2]. According to the author's knowledge the parameter $\xi$ appeared the first time in [2] just to fix the range of temperature as was explained above.

Generally, the dynamical criterium for freeze-out was formulated as the moment when the local velocity of the rarefaction due to the expansion overcomes the local thermal velocity [33]. Since the freeze-out means the end of collisions the criterium can be stated more precisely as the moment at a space point when the average local proper time between subsequent collisions $\tau_{\mathrm{scatt}}$ overcomes the characteristic time for expansion of the system given by $\tau_{\mathrm{exp}} = V/\dot{V}$, where $\dot{V}$ denotes the derivative of the volume of the system with respect to the local proper time. The expansion characteristic time is the time which the evolution of the system from very small volume (almost zero) to the given volume $V$ would take with the constant speed equal to the local velocity $\dot{V}$. For a given hadron species the scattering time can be estimated as $\tau_{\mathrm{scatt}} = \lambda/\upsilon_{\mathrm{th}} = 1/\rho_{\mathrm{tot}}\sigma_{\mathrm{tot}}\upsilon_{\mathrm{th}}$, where $\lambda$ is the mean free path, $\rho_{\mathrm{tot}}$ is the total density of all particles, $\sigma_{\mathrm{tot}}$ is the average cross section and $\upsilon_{\mathrm{th}}$ is the average thermal velocity [34,35]. The characteristic expansion time can be expressed as $\tau_{\mathrm{exp}} = (\partial_\mu u^\mu)^{-1} = V/\dot{V}$ [36].

Hydrodynamics can be applied for $\tau_{\mathrm{scatt}} \ll \tau_{\mathrm{exp}}$ but when $\tau_{\mathrm{scatt}} \gg \tau_{\mathrm{exp}}$ certainly the system is not in statistical and thermal equilibrium [37]. However, the determination of the strict border between a flow and a free stream of particles is somehow arbitrary, it is commonly accepted that on this border $\tau_{\mathrm{scatt}} \sim \tau_{\mathrm{exp}}$. Both times increase when the system cools down, but $\tau_{\mathrm{scatt}}$ is growing steeper, so it cuts $\tau_{\mathrm{exp}}$ at some temperature (it represents the case

$\xi = 1$; for some examples of simulations of $\tau_{\rm scatt}$ and $\tau_{\rm exp}$ see Ref. [35]). In terms of rates $\tau^{-1}_{\rm scatt}$ is falling steeper and cuts $\tau^{-1}_{\rm exp}$ at some temperature. For the expansion rate multiplied by $\xi$, if $\xi < 1$ then $\xi\tau^{-1}_{\rm exp}$ cuts $\tau^{-1}_{\rm scatt}$ at some lower temperature, if $\xi > 1$ it happens at some higher temperature. Therefore, the choice $\xi = 0.295$ as in [2] means decreasing the freeze-out temperature so as it falls into the blast-wave range. Thus it is very likely that increasing $\xi$ but still keeping $\xi \sim 1$ one could obtain the freeze-out temperature in the range of $T_{\rm kin} \simeq 140$–$165\,{\rm MeV}$ as in the present model. Another point is the centrality dependence of $T_{\rm kin}$. The change of $T_{\rm kin}$ with the centrality, of the order of 25% between the most central and the most peripheral bins, was obtained from Eq. (12) with the same expression for $\tau^{-1}_{\rm scatt}$ taken for all centrality classes [2]. Such assumption might not be reasonable, since *e.g.* in Ref. [38] variation of the temperature dependence of $\tau_{\rm scatt}$ with specific entropy $S/A = s/n_{\rm B}$ (entropy density per baryon number density) was shown, see Fig. 7 there. The specific entropy, as an initial condition, could be different for each centrality class, so the different expression for $\tau^{-1}_{\rm scatt}$ should be put into Eq. (12) in each case. Moreover, the scattering rate was calculated for pions only in a pion–kaon mixture [37]. The full scattering rate should include interactions between all constituents of the gas. Of course, this is an open question how such realistic scattering rate could influence the centrality dependence of $T_{\rm kin}$ determined from Eq. (12), but that this might flatten the dependence cannot be excluded. And the last remark, $T_{\rm kin}$ points described as the STAR data [9] in Fig. 3 of Ref. [2] are not the measured quantities. They are blast-wave-fit results. Thus Fig. 3 in [2] demonstrates that $T_{\rm kin}$ obtained within the model where the freeze-out takes place on a hypersurface of constant temperature is consistent with the average $T_{\rm kin}$ for the hypersurface in which the temperature is not constant.

In summary, the alternative hydrodynamical model has been proposed to describe hadronic $p_{\rm T}$ spectra measured at relativistic heavy-ion collisions. So far, conclusions about chemical and thermal (kinetic) freeze-outs have been drawn from the blast-wave parametrization [18] of the final stage of the collision. It has turned out that those conclusions are not definite and depend strongly on the applied model. In the present model the temperature and the baryon number chemical potential fitted to the spectra are almost independent of the centrality of the collision and their values are very close to the values at the chemical freeze-out, what is opposite to the conclusions drawn from the blast-wave model analysis [2]. Such behavior justifies the *ad hoc* assumption about one freeze-out postulated in Refs [22, 23].

This work was supported in part by the Polish Ministry of Science and Higher Education under contract No. N N202 0953 33.

## REFERENCES


[1] U. Heinz, *Nucl. Phys.* **A661**, 140 (1999).

[2] U. Heinz, G. Kestin, *PoS* **CPOD2006**, 038 (2006) [arXiv:nucl-th/0612105].

[3] G. Torrieri, J. Rafelski, *J. Phys. Conf. Ser.* **5**, 246 (2005) [arXiv:hep-ph/0409160].

[4] M. Kaneta, N. Xu, presented at QM2004, Oakland, arXiv:nucl-th/040506.

[5] W. Florkowski, W. Broniowski, M. Michalec, *Acta Phys. Pol. B* **33**, 761 (2002).

[6] J. Cleymans, B. Kampfer, M. Kaneta, S. Wheaton, N. Xu, *Phys. Rev.* **C71**, 054901 (2005).

[7] P. Braun-Munzinger, D. Magestro, K. Redlich, J. Stachel, *Phys. Lett.* **B518**, 41 (2001).

[8] J. Rafelski, J. Letessier, G. Torrieri, *Phys. Rev.* **C72**, 024905 (2005).

[9] [STAR Collaboration] J. Adams *et al.*, *Phys. Rev. Lett.* **92**, 112301 (2004).

[10] [STAR Collaboration] O.Y. Barannikova, presented at QM2004, Oakland, arXiv:nucl-ex/0403014.

[11] [STAR Collaboration] O. Barannikova, *J. Phys. G* **31**, S93 (2005).

[12] A. Baran, W. Broniowski, W. Florkowski, *Acta Phys. Pol. B* **35**, 779 (2004).

[13] P. Braun-Munzinger, K. Redlich, J. Stachel, in *Quark-Gluon Plasma 3*, Eds R.C. Hwa and Xin-Nian Wang, World Scientific Publishing, Singapore 2004, p. 491.

[14] [PHENIX Collaboration] K. Adcox *et al.*, *Phys. Rev.* **C69**, 024904 (2004).

[15] [PHENIX Collaboration] J.M. Burward-Hoy, *Nucl. Phys.* **A715**, 498 (2003).

[16] [BRAHMS Collaboration] I. Arsene *et al., Phys. Rev.* **C72**, 014908 (2005).

[17] [PHOBOS Collaboration] B.B. Back *et al., Phys. Rev.* **C75**, 024910 (2007).

[18] E. Schnedermann, J. Sollfrank, U. Heinz, *Phys. Rev.* **C48**, 2462 (1993).

[19] W. Broniowski, A. Baran, W. Florkowski, *Acta Phys. Pol. B* **33**, 4235 (2002).

[20] J. Cleymans, H. Oeschler, K. Redlich, *J. Phys. G* **25**, 281 (1999) [arXiv:nucl-th/9809031].

[21] J. Cleymans, K. Redlich, *Phys. Rev.* **C60**, 054908 (1999) [arXiv:nucl-th/9903063].

[22] W. Broniowski, W. Florkowski, *Phys. Rev. Lett.* **87**, 272302 (2001).

[23] W. Broniowski, W. Florkowski, *Phys. Rev.* **C65**, 064905 (2002).

[24] [Particle Data Group Collaboration] K. Hagiwara *et al.*, *Phys. Rev.* **D66**, 010001 (2002).

[25] J.D. Bjorken, *Phys. Rev.* **D27**, 140 (1983).

[26] F. Cooper, G. Frye, E. Schonberg, *Phys. Rev.* **D11**, 192 (1975).

[27] M. Chojnacki, W. Florkowski, T. Csörgö, *Phys. Rev.* **C71**, 044902 (2005).

[28] D. Prorok, *Eur. Phys. J.* **A24**, 93 (2005).

[29] [PHENIX Collaboration] S.S. Adler *et al.*, *Phys. Rev.* **C69**, 034909 (2004).
[30] D. Prorok, *Phys. Rev.* **C73**, 064901 (2006).
[31] [STAR Collaboration] J. Adams *et al.*, *Phys. Rev. Lett.* **98**, 062301 (2007).
[32] J. Rafelski (private communication).
[33] J.P. Bondorf, S.I.A. Garpman, J. Zimanyi, *Nucl. Phys.* **A296**, 320 (1978).
[34] K.S. Lee, M.J. Rhoades-Brown, U.W. Heinz, *Phys. Rev.* **C37**, 1463 (1988).
[35] G. Bertsch, M. Gong, L.D. McLerran, P.V. Ruuskanen, E. Sarkkinen, *Phys. Rev.* **D37**, 1202 (1988).
[36] K.J. Eskola, H. Niemi, P.V. Ruuskanen, *Phys. Rev.* **C77**, 044907 (2008) [arXiv:0710.4476 [hep-ph]].
[37] C.M. Hung, E.V. Shuryak, *Phys. Rev.* **C57**, 1891 (1998).
[38] E. Schnedermann, U.W. Heinz, *Phys. Rev.* **C50**, 1675 (1994).